Ocean Engineering 87 (2014) 1–9

Contents lists available at ScienceDirect

Ocean Engineering

journal homepage: www.elsevier.com/locate/oceaneng

Unsteady RANS computations of flow around a circular cylinder for a wide range of Reynolds numbers

R.M. Stringer [a,*], J. Zang [a], A.J. Hillis [b]

[a] Department of Architecture and Civil Engineering, University of Bath, Bath BA2 7AY, UK
[b] Department of Mechanical Engineering, University of Bath, Bath BA2 7AY, UK

ARTICLE INFO

Article history:
Received 5 April 2013
Accepted 19 April 2014

Keywords:
CFD
Cylinder
OpenFOAM
Tidal
URANS
VIV

ABSTRACT

A methodology for computation of flow around circular cylinders is developed and tested using prominent commercial and open-source solvers; ANSYS® CFX-13.0 and OpenFOAM® 1.7.1 respectively. A range of diameters and flow conditions are accounted for by generating solutions for flows at Reynolds numbers ranging from 40 to 10^6. To maintain practical solve times a 2D Unsteady Reynolds-Averaged Navier–Stokes (URANS) approach is taken. Furthermore, to maximise accuracy a tightly controlled meshing methodology, suitable adaptive timestepping, and appropriate turbulence modelling, are assembled. The resulting data is presented for lift and drag forces, Strouhal frequency, time accuracy and boundary layer correlation. Despite closely matching case definitions, significant differences are found in the results between solvers; OpenFOAM displays high correlation with experimental data at low to sub-critical values, whereas ANSYS proves to be more effective in the high sub-critical and critical regions. This variance demonstrates the sensitivity of the case to solver specific mathematical constraints and that for practical engineering a parameter study is essential. By removing many common variances associated with grid and transient components of URANS computations the developed methodology can be used as a benchmark case for further codes solving cylindrical structures.

1. Introduction

Understanding the flow around a circular cylinder has historically been a fundamental challenge for researchers, largely due to the complexity and transient nature of the wake. However, in the last decade, desktop computational resources have increased sufficiently such that high resolution solutions for practical engineering have become feasible. One such application, the motivation for the study, is the use of cylindrical geometries as structural members and pipelines in offshore applications. This usage is particularly relevant due to the exploitation of new renewable energy technologies both wind and marine, many of which include cylindrical features in some form. Analysis of circular cylinders for the offshore market has been primarily to assess structural loading caused by vortex shedding. This phenomenon has influenced new offshore technologies aimed at reducing the impact of vortex induced vibration (VIV) on structural elements such as riser fairings and platform leg surfacing. In the context of marine renewables, it is also possible that vortices shed from cylindrical components may reduce device efficiency and therefore require an increased level of resolution in design and development solutions. To address this, this research aims to develop and assess a rigorous numerical methodology for modelling such cases.

The flow around cylinders has been extensively investigated through experimentation by notable contributors such as Tritton (1959), Roshko (1955) and Achenbach (1968), amongst many others. One of the key outcomes of this work was to categorise flow by regimes of vortex shedding with Reynolds number (Re), given in Eq. (1). A prominent early paper by Lienhard (1966) proposes an outline of flow characteristics from laminar flow, up to supercritical values $\approx \mathrm{Re}\ 3.5 \times 10^6$. However, the complexity of the turbulent wake has undergone many new discoveries, with a distinct contribution from advancing numerical modelling. A review by Williamson (1996) considers the wake in detail; highlights include a detailed account of the transition of wakes from 2D to 3D in the range $180 < \mathrm{Re} < 190$, control of the shedding by modification of the cylinder end conditions, and the Direct Numerical Simulation (DNS) of 3D instabilities in landmark detail. The regimes of flow around a cylinder as Reynolds number increases have been refined by numerous researchers, most notably Zdravkovich (1990) with 15 distinct ranges. A summary of the key stages in flow development are presented in Table 1.

The study here considers incremental values of Re from 40 up to a maximum of 10^6. To give a perspective on the range, the peak

* Corresponding author.
E-mail address: r.m.stringer@bath.ac.uk (R.M. Stringer).

http://dx.doi.org/10.1016/j.oceaneng.2014.04.017
0029-8018/

Table 1
Flow regimes around a circular cylinder (Raghavan and Bernitsas, 2011).

Re range	Flow regime
$Re < 1$	Creeping flow
$3–5 < Re < 30–40$	Steady separation (Foppl vortices)
$30–40 < Re < 150–300$	Laminar periodic shedding
$150–200 < Re < 1.4 \times 10^5$	Subcritical
$1.4 \times 10^5 < Re < 1 \times 10^6$	Critical
$1 \times 10^6 < Re < 5 \times 10^6$	Supercritical
$5 \times 10^6 < Re < 8 \times 10^6$	Transcritical
$8 \times 10^6 < Re$	Postcritical

value of Re is equivalent to a 0.5 m pile in a 2 m/s tidal flow. This velocity range represents 'slack water' up to the peak flow/ebb for many locations around the UK, such as the Severn Estuary (Xia et al., 2010).

1.1. Numerical literature

At practical Reynolds numbers the wake and vortex formation around a circular cylinder is preclusively complex to fully compute, therefore a suitable level of spatial and temporal simplification has to be found. While it is known that 3D structures are common in the wake of circular cylinders, simplification of the case to 2D has been employed in the present research based on successful results obtained by a number of researchers.

Beginning with low Re cases, $Re < 160$, Park et al. (1998) and Dehkordi and Jafari (2009) both obtain excellent agreement with experimental values for all parameters monitored using a laminar URANS method; no ill effects from 2D simplification are found. Moving into the subcritical regime, research conducted by Rahman et al. (2008) compares a number of two-equation turbulence models at Re values of 1000 and 3900. Rahman et al.'s results show a clear improvement in accuracy using the shear stress transport model (SST) over the $k-\varepsilon$ and realizable $k-\varepsilon$ models. At critical and supercritical Re values of 10^6 and 3.6×10^6, Ong et al. (2009) evaluated the $k-\varepsilon$ model with a log law wall function. A limited study of the effect of y^+ was conducted although values are kept in the 5–30 region. Ong et al. compare their results with 2D and 3D Large Eddy Simulation (LES) and experimental data, with force and shedding frequencies falling within known limits. However, the pressure distribution and shear stress show some divergence. Benim et al. (2007) explored the topic of near wall meshing further by using the commercial code FLUENT to compute flow around a cylinder at $Re = 10^4$ using wall models and the standard $k-\varepsilon$ turbulence model. Benim et al.'s results from meshes in the range of y^+ values, from 10 to 1000, yielded a large range of drag values. Significantly no discernible plateau is visible. Consequently, the author continued testing without wall functions, switching to the SST turbulence model and adhering to meshes that conform to $y^+ = 1$. It is worth noting that a non-conformal surface grid is used, akin to a body fitted quadtree grid. In parallel with Ong et al., Benim et al. found acceptable correlation in the supercritical regime but this rapidly loses accuracy in the critical transition region, under-predicting values quantitatively for both $k-\varepsilon$ and, to a lesser extent, SST models. Tutar and Holdo (2001) computed results for the 2D case in both URANS and LES models at an Re of 1.4×10^5. Their results show that a non-linear two-equation $k-\varepsilon$ model gives improvement over the standard form, although both URANS methods under-predict pertinent values. LES is seen to produce a superior flow field, as expected, but results in over-prediction of force and shedding values compared with experiment. While LES in this case used a fully resolved boundary layer, the URANS method used wall models that have previously been shown to be highly mesh-dependent.

Based on the findings discussed here and additional sources, it can be concluded that the URANS method shows great promise for satisfactory prediction of flow characteristics around circular cylinders. However, the lines of applicability are blurred in terms of Reynolds number range and optimal computational methodology. This paper presents a rigorous methodology to overcome these limitations and to maximise the quality of URANS simulation. The methodology incorporates the SST turbulence model, a fully resolved boundary layer at every Re, a dense conformal grid, cell aspect ratio control and adaptive timestepping. Two solvers are used to compare the effects of the two host software packages, particularly as each uses alternative mathematical approaches.

The two software packages selected for the study are OpenFOAM 1.7.1 (OpenFOAM) and ANSYS® CFX-13.0 Academic Research (CFX). OpenFOAM is a C++ based open-source software written for the Linux platform, while CFX is a prominent commercial code heavily used in the aerospace and marine industries amongst others. Both OpenFOAM and CFX employ the finite volume method (FVM) to represent and solve the Navier–Stokes equations in algebraic form; Table 2 gives a basic outline of the contrasting approaches taken by the two solvers.

OpenFOAM has numerous FVM solvers depending on application, and for incompressible transient problems the pisoFoam solver is the most suitable. As the title suggests, pisoFoam uses the Pressure Implicit with Splitting of Operators method for pressure–velocity coupling proposed by Issa (1986). The method is akin to the SIMPLE (Semi-Implicit Method for Pressure-Linked Equations) algorithm with the addition of a second corrector stage that performs momentum (neighbor) and skewness correction. Note that all future references to OpenFOAM are specifically in regard to the implementation of the pisoFoam solver. As Table 1 states, OpenFOAM perfoms the PISO loop as part of the segregated solution method, while CFX uses a coupled solution, where continuity, momentum and energy are solved simultaneously and hence decoupling is avoided by using Rhie–Chow pressure interpolation. One of the key differences between the two methods is their sensitivity to timestepping. The coupled method in CFX is able to re-solve the governing equations in a pseudo inner timestep, whereas OpenFOAM converges each parameter once, correcting only for pressure and velocity in each timestep. The result is that CFX is relatively insensitive to timestep, while OpenFOAM requires tight control, such as adhering to low Courant numbers. In terms of spatial discretisation, the medium dual-method adopted by CFX divides the original mesh into a new set of polyhedral volumes defined by connecting the face centroids and edge midpoints of all cells that share any single grid node. In contrast, the cell centered method uses the existing cell volumes defined by the input mesh. The result is that CFX includes a greater number of integration points, while OpenFOAM retains a greater level of flexibility. A comprehensive comparison of the methods is offered by Blazek (2005).

Turbulence models are used equally for both solvers such that cases considered to have globally low Re employ a laminar model,

Table 2
Comparison of mathematical attributes for CFX and OpenFOAM.

Attribute	CFX	OpenFOAM[a]
Solution method	Fully coupled	Segregated
Temporal control	Implicit	Implicit/explicit
Discretisation	Median-dual cell-vertex	Cell-centred
Variable storage	Collocated	Collocated
Pressure–velocity handling	Rhie–Chow (adapted)	PISO

[a] Attributes specific to pisoFoam module.

whereas turbulent flows, Re > 150, implement the Shear Stress Transport turbulence model (SST), as developed by Menter (1994). The model uses a $k-\omega$ model to estimate turbulence in the near wall region and $k-\varepsilon$ outside the boundary layer; a blending function connects the two models. The SST model has been chosen for the study due to its availability in both solvers and a history of preferable results in high shear conditions, demonstrated by Bardina et al. (1997), over alternative mainstream models.

In terms of iterative method and general interpolation of the variables, both solvers have been kept to settings suggested by their accompanying literature. In OpenFOAM this comprises Gaussian methods for gradient divergence and Laplacian schemes, with second order accuracy throughout. Both preconditioned conjugate gradient and bi-conjugate gradient solvers are used for solution of the physical and turbulence parameters as found in example pisoFoam models. CFX uses a proprietary method which is described at length by Gretton (2009). While a comprehensive account of the setup is provided in the next section, any omissions regarding underlying constants should be assumed to be solver default values.

2. Numerical method

In this section a detailed account of the setup is given, including boundary and solver constraints, meshing strategy and turbulence modelling. The dimensions of the domain for all cases are given in Fig. 1. The proportions are analogous to those of previous publications, including Ong et al., and Rahman et al. where blockage is rendered negligible; also note that the 3rd dimension (z) was set to 0.1D.

2.1. Boundary conditions

The boundary conditions for all cases were defined in OpenFOAM and CFX with similarity as a stringent objective. The properties are as follows.

2.1.1. Inlet

A uniform flow is specified at the inlet, whose Reynolds number is given by Eq. (1), for flow velocity U, where ρ is density, D is diameter and μ is dynamic viscosity.

$$Re = \frac{\rho U D}{\mu} \tag{1}$$

2.1.2. Outlet

The outlet is sufficiently downstream such that any vortices are not yet present in the flow stream. In this case a pressure or velocity outlet is applicable with both showing identical results. For a pressure boundary in CFX the relative pressure is set to zero; $P_{rel} = 0$. In OpenFOAM the equivalent setting used is a 'free stream' pressure outlet.

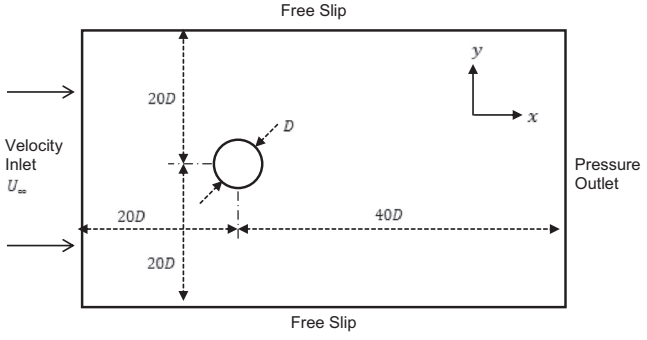

Fig. 1. Geometry of the computed domain (not to scale).

2.1.3. Free slip edges

The sides assigned as 'free-slip' boundaries, shown in Fig. 1, allow the fluid velocity component parallel to the wall to be computed, while velocity normal to the wall and the wall shear stress are set to zero; $U_y = 0$, $\tau_{wall} = 0$.

2.1.4. Periodic faces

The boundaries in the X–Y plane were set as symmetry planes; here velocities and pressures are assumed equal at both sides of the boundary. With zero spanwise flow in the 2D case, this boundary type provides the illusion of an infinitely long cylinder. CFX employs this technique due to its node centred spacial discretisation, the result being a very narrow 3D calculation, sometimes regarded as '2.5D'. In OpenFOAM a second option exists in the form of an 'empty' boundary condition. In this case the solver performs an effective 2D calculation between cell centres, with a result existing only within a central plane. Tests were conducted in OpenFOAM for both symmetry and empty boundaries, returning a result of negligible difference.

2.1.5. Cylinder surface

The cylinder boundary is set to a no-slip condition, where pressure is set to zero gradient and velocities are set to zero, $U_x = U_y = 0$.

2.2. Turbulence properties

For URANS computation using the SST model, as discussed in Section 1.1, values for turbulence kinetic energy k and turbulent frequency ω are required. In CFX it is standard practice to select a turbulence intensity from which automatic values are calculated; however, in the interests of similarity both solvers are manually set using Eqs. (2) and (3). A turbulence intensity I of 2.5% is used throughout; note that turbulence length l is given in (4) and C_μ is the empirical non-dimensional constant 0.09. Values of k and ω at the cylinder wall are given in Eqs. (5) and (6), as proposed by Wilcox (1993), where v is kinematic viscosity, $\beta = 0.075$, a non-dimensional constant and y_1 is the distance to the first node:

$$k = \frac{3}{2}(U_\infty I)^2 \tag{2}$$

$$\omega = \frac{k^{\frac{1}{2}}}{kC_\mu l} \tag{3}$$

$$l = 0.07D \tag{4}$$

$$k_{wall} = 0 \tag{5}$$

$$\omega_{wall} = \frac{60v}{\beta y_1^2} \tag{6}$$

It is important to note that the use of standard logarithmic wall functions for low Re meshes leads to high inaccuracies. Kalitzin et al. (2005) discuss the issues in detail, including both methods employed in this work. The CFX solver uses an automatic near-wall treatment in which k is set to zero and the velocities close to the wall are calculated from an alternative formulation of the velocity profile. Additionally the ω term is a blended value of sublayer and logarithmic components. The SST model available for pisoFoam in the employed version of OpenFOAM forces the implementation of a wall model and does not offer an advanced solution as found in CFX. However, it is possible to gain an effective solution by replacing the standard logarithmic model with a continuous wall

formulation; in this case Spalding's solution to the 'law of the wall' is used (Spalding, 1961).

2.3. Meshing

To assure a high level of grid independence a low-Re approach to meshing is taken. The term 'low-Re' is not to be confused with global Reynolds number, but indicates the low turbulent Reynolds number that exists in the viscous sublayer. The y^+ value represents a non-dimensional distance of the first node from a no-slip wall. It links the node distance to shear stress τ_ω, by non-dimensionalising the value with the fluid properties density and viscosity—refer to Eq. (7). In order to utilise low-Re boundary properties it is generally accepted that the mesh must achieve first layer cell thicknesses equivalent to $y^+ < 1$ for most solvers, see ANSYS® (2010) and Benim et al. (2007). However, a study of hull forms in comparably high Re marine flows by Jagadeesh and Murali (2009) concludes that a mesh of $y^+ < 2$ with 5 cells in the boundary layer was sufficient for accurate solution of a number of two-equation turbulence models.

$$y^+ = \frac{\sqrt{\tau_\omega/\rho}\, y_1}{\nu} \tag{7}$$

To achieve a mesh within the constraints identified, a commonly employed empirical calculation based on flat plate theory is initially used, as follows:

$$y_1 = Dy^+ \times \sqrt{74} Re_L^{-13/14} \tag{8}$$

Initial tests were conducted using the predicted values and post-processed to acquire boundary layer thicknesses using velocity at $0.99U_\infty$. The result was a clear over-prediction for thickness y_1, particularly at walls adjacent to the maximum flow velocities. Therefore a second round of meshing was completed which ensured that a minimum 5 cells were located in the boundary layer; for the majority of the cylinder surface this number was higher. To assess and correct the inflated hexahedral mesh layers, equations were derived to link total height (of boundary layer) h, number of layers c, expansion ratio r and first cell height y_1. Eqs. (9)–(11) represent the derivation of the total thickness, and Eqs. (12) and (13) are rearrangements for post-processing the number of layers and establishing a replacement first cell thickness respectively. Note that the final meshes conformed to a maximum value of $0.5 < y^+ < 1.5$ on post-processing.

$$h = y_1 + y_1 r + y_1 r^2 + y_1 r^3 + \ldots + y_1 r^{c-1} \tag{9}$$

$$h = \sum_0^{c-1} y_1 r^c \tag{10}$$

$$h = y_1 \left(\frac{r^c - 1}{r - 1} \right) \tag{11}$$

$$c = \frac{\ln\left(\frac{h(r-1)+y_1}{y_1} \right)}{\ln r} \tag{12}$$

$$y_1 = h \left(\frac{r - 1}{r^c - 1} \right) \tag{13}$$

An exact mesh match between the two solvers was maintained by generating all meshes in ANSYS® Meshing 13.0 and then converting into OpenFOAM format for each Reynolds number. The mesh template consists of a body fitted hexahedral region surrounding the cylinder with unstructured wedges filling the remaining far field domain. A typical mesh in the near field of the cylinder is shown in Fig. 2 (left). The lack of any symmetry is theoretically unimportant given sufficient grid resolution, a positive aspect being that it aids the development of vortex shedding. Iaccarino et al. (2003) conducted a URANS simulation of a square cylinder in an external flow, reporting that for a symmetrical grid a user induced flow velocity perturbation was required to induce shedding. Fig. 2 (right) shows the body fitted region of the mesh in more detail; an expansion ratio of 1.1 is used with a total of 30 layers. Furthermore, the aspect ratio of wall cell circumferential width to cell height y_1 is kept below 20:1 for all cases; the single exception is $Re = 10^6$ where the ratio is extended to 100:1, a value that still offers exceptional resolution at this Re.

2.4. Solver control

Both CFX and OpenFOAM are implicit solvers; however, the pisoFoam solver does not include outer loop corrections, i.e. recalculation of the N–S equations at any given timestep. The result is that a low Courant number is required to maintain numerical stability, calculation of which is given in Eq. (14), where Δt is the timestep and Δx is the minimum cell width. As a consequence the timestep decreases significantly as the mesh is refined for greater Reynolds numbers and hence processing time increases disproportionally. It should be noted that pisoFoam does not include Courant controlled timestepping by default; therefore

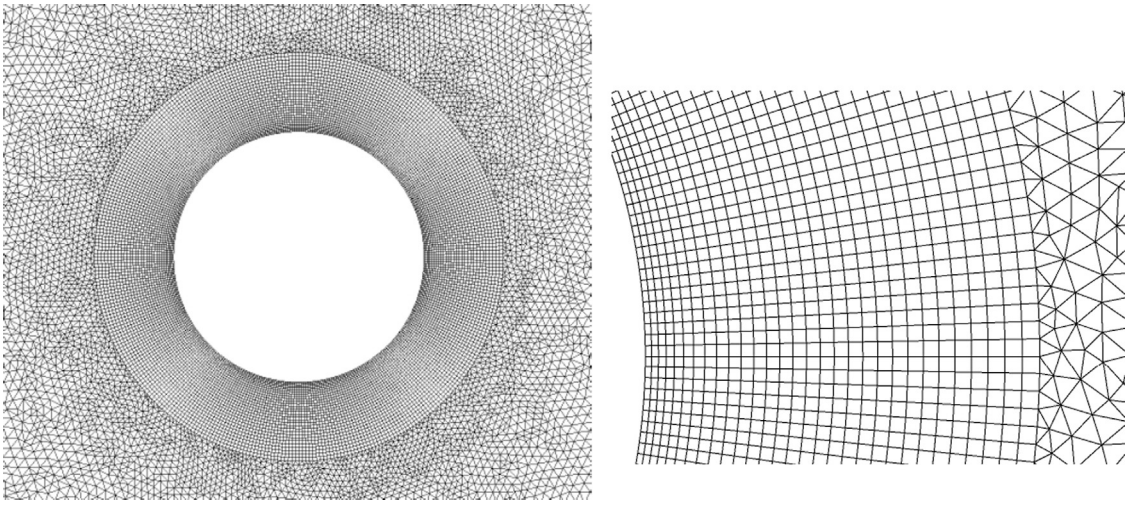

Fig. 2. Images of a typical mesh (Re = 1000 shown); Left: Image showing near and far field meshes from the cylinder, Right: Detail of inflated hexahedral mesh at the cylinder boundary.

modifications to the source code are required.

$$Cr = \frac{U\Delta t}{\Delta x} \tag{14}$$

The second important aspect of solver control is the convergence criteria. Both CFX and OpenFOAM include residual calculations for the solution variables, mass, momentum and turbulence parameters in the case of CFX and pressure, velocity and turbulence in the case of OpenFOAM. The recommended value for both CFX and the pisoFoam solver in accompanying guidance notes is 10^{-6} for tight convergence; this value is selected for all cases, as well as solving all parameters to double precision.

The specified total time is calculated from a non-dimensional time value t^* as given in Eq. (15). All simulations are solved to 150 non-dimensional time units.

$$t^* = \frac{tU}{D} \tag{15}$$

2.5. Post-processing

Data from CFX and OpenFOAM were post-processed using ANSYS CFD-Post 13.0 and ParaView 3.12.0-RC2 respectively. Instantaneous values of drag coefficient C_D and root mean square of lift coefficient C_{Lrms} are calculated using Eqs. (16) and (17), where F_D and F_L are the corresponding unit forces. The Strouhal number (St) represents a normalised value of shedding frequency; see Eq. (18), where f is the shedding frequency in Hz. The coefficient of pressure p_∞ is calculated by Eq. (19), where p is the static pressure, and where all values with the subscript infinity denote free-stream values taken 0.1 m from the inlet on the x-axis and at the centreline of the cylinder on the y-axis:

$$C_D = \frac{F_D}{0.5\rho U^2 D} \tag{16}$$

$$C_{Lrms} = \frac{\sqrt{\frac{1}{n}(F_{L_1}^2 + F_{L_2}^2 + \ldots + F_{L_n}^2)}}{0.5\rho U^2 D} \tag{17}$$

$$St = \frac{fD}{U} \tag{18}$$

$$C_p = \frac{p - p_\infty}{\frac{1}{2}\rho_\infty U_\infty^2} \tag{19}$$

3. Results and discussion

To represent the full range of conditions expected in the case of a cylinder in tidal flow, computations have been performed at Re=40, 100, 10^3, 10^4, 10^5 and 10^6. The following results serve to evaluate a number of objectives, namely, the performance of URANS simulation using the Menter SST turbulence model combined with low-Re meshing, and the comparability of the commercial code ANSYS® CFX 13.0 with the open-source code OpenFOAM (using the pisoFoam solver), given nominally identical cases. A number of key parameters have been identified for presentation and discussion.

3.1. Calibration testing Re=40

Testing initially at a low Reynolds number using a laminar model was conducted to provide validation of the boundary setup strategy outlined throughout Section 2 (excluding turbulence), and to evaluate the success of the modified pisoFoam solver to include Courant timestepping control. The Courant number is initially defined as 0.8.

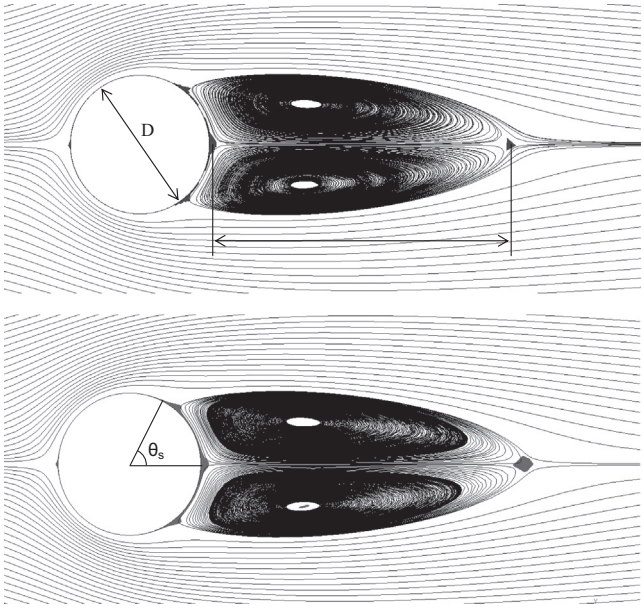

Fig. 3. Streamline and stagnation point images at Re=40 after 150 non-dimensional seconds, Top: OpenFOAM, Bottom: CFX.

Table 3
Lift, drag and separation geometries for Re=40. Experimental: Tritton (1959); Taneda (1956); Coutanceau and Bouard (1977); Grove et al. (1964); Numerical: Dehkordi and Jafari (2009), Park et al. (1998), Dennis and Chang (1970).

	C_D	C_{Dp}	C_{Df}	L/D	θ_s
Experimental	1.6	0.935	–	2.1–2.19	53–53.4
Numerical	1.51–1.54	0.99–1.02	0.51–0.54	2.15–2.345	53.6–53.8
CFX	1.55	1.01	0.54	2.25	54
OpenFOAM	1.55	1.01	0.54	2.17	54

The images in Fig. 3 show the visible similarity between the Foppl votices computed by OpenFOAM and CFX at Re=40. The images were generated by independent post-processing software; (a) Paraview and (b) ANSYS® 13.0 CFD-Post. Comparing the results quantitatively at $t^*=150$, shown in Table 3, the components of drag, wake length to cylinder diameter ratio (L/D) and separation angle (θ_s) are all within minor tolerances among CFX, OpenFOAM and experimental values.

Although the tests were continued up to $t^*=150$, the results of both CFX and OpenFOAM had effectively reached a steady state around $t^*=30$, with the majority of the wake growth occurring below $t^*=12$. Fig. 4 displays the time histories of wake growth for both the computed cases and those from literature.

For both CFX and OpenFOAM the wake growth is almost identical to that computed by Rosenfeld, and only marginally less than experimental values at 12 s. The agreement between the present study calculations of both CFX and OpenFOAM and the published data indicates that the cases are appropriately defined and that the Courant number value of 0.8 is an acceptable initial value for time accurate computation. Using this information the remaining tests were defined, including one further laminar shedding case at Re=100, and a number of turbulent cases using the SST turbulence model from Re 10^3 to 10^6. The results of these tests are graphically represented and discussed in terms of forces and flow features henceforth.

3.2. Drag coefficient

The results for drag coefficient averaged over $t^*=140$–150 for both solvers are plotted in Fig. 5 against published work by

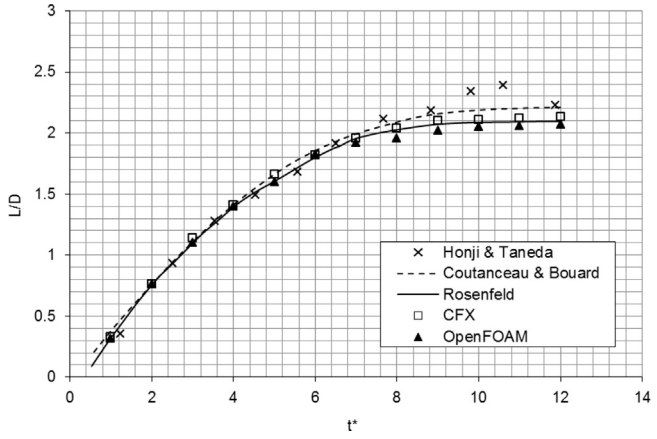

Fig. 4. Development of vortex length with respect to non-dimensional time. Experimental: Honji and Taneda (1969); Coutanceau and Bouard (1977); Numerical: Rosenfeld and Kwak (1988).

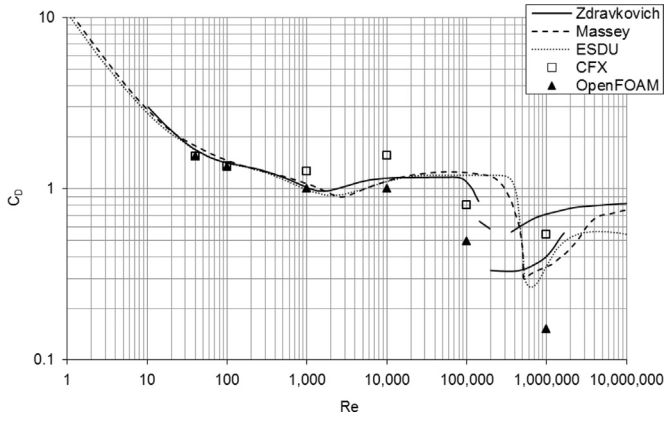

Fig. 5. Drag coefficient versus Reynolds number; correlation between experimental and numerical results. Published values for smooth cylinder: Zdravkovich (1990), Massey (1989) and ESDU (1980).

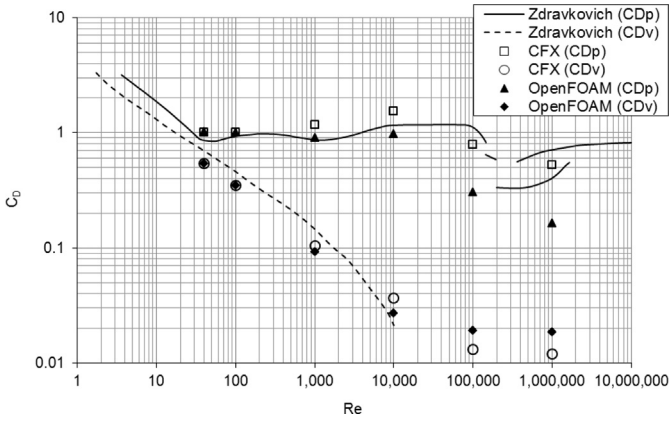

Fig. 6. Pressure and viscous components of drag coefficient versus Reynolds number. Published values for smooth cylinder: Zdravkovich (1990).

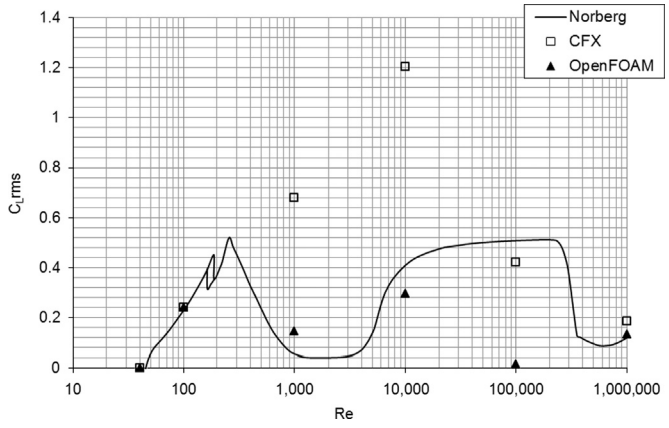

Fig. 7. Graph of rms value of lift coefficient with Reynolds number. Published experimental data: Norberg (2003).

Zdravkovich (1990), Massey (1989) and the Engineering Sciences Data Unit (ESDU, 1980). The three reference plots are considered to be an infinitely long smooth cylinder. The discrepancy between the plots in the critical region, around $10^5 < \mathrm{Re} < 3.5 \times 10^6$, is demonstrative of the flow instability in this region with experimental values varying significantly among many authors. The plot by Massey is largely similar to that of Wieselsberger (1923), while Zdravkovich identifies the large variance by including boundaries of possible results, such as that presented by Shih et al. (1993). The ESDU source largely affirms Massey and Zdravkovich's findings.

The present results from CFX and OpenFOAM are clearly in agreement at low Re values; in fact, OpenFOAM continues to give values within $0.1C_D$ of experimental values up to $\mathrm{Re}=10^4$. CFX over-predicts C_D at Re values of 10^3 and 10^4, but shows some recovery in the critical region, that of $\mathrm{Re} > 10^5$, with values close to, or within, known regions of high variability. In the same region OpenFOAM suffers a sharp drop in drag; to investigate this, a breakdown of the result into pressure and viscous components is presented in Fig. 6.

Considering firstly the viscous element of drag, values are generally under-predicted by both solvers, with values above $\mathrm{Re}=10^3$ becoming negligible compared to total drag. The comparative importance of pressure drag is clearly visible, which in the CFX results shows good correlation with experimental values for all Re values although quantitatively it reaches a maximum error $\approx 30\%$ at $\mathrm{Re}=10^4$. OpenFOAM displays similar characteristics up to $\mathrm{Re}=10^4$, where the maximum error is half at approximately 15%. Above this Re the OpenFOAM result clearly shows the extensive under-prediction of pressure drag.

3.3. Lift coefficient

A significant contribution to the distribution of pressure driven forces is that of vortex shedding, an expected feature of the flow at the Reynolds numbers tested (with the exception of $\mathrm{Re}=40$). The fluctuating lift coefficient, C_L', provides an accessible record of vortex shedding. Taking a root mean squared (rms) of values for time $t^*=140$–150, see Eq. (17), results are plotted alongside a best fit curve based on an experimental review by Norberg (2003) in Fig. 7. In parallel to the trends in C_D, OpenFOAM performs reasonably up to $\mathrm{Re}=10^4$ with results falling within the scatter of the original data points presented by Norberg (not shown in Fig. 7). At $\mathrm{Re}=10^5$ OpenFOAM is seen to generate zero lift, suggesting the absence of shedding, followed by a final value at $\mathrm{Re}=10^6$ recovering to closely match Norberg's result. The CFX results differ significantly from those of OpenFOAM in the subcritical region with highly overpredicted values at $\mathrm{Re}=10^3$ and $\mathrm{Re}=10^4$. At high Re the CFX results for C_{Lrms} return to values with less than a 15% error from Norberg's result. This unusual behaviour in the critical Re range can be investigated further by considering the lift oscillation, represented by the Strouhal shedding frequency.

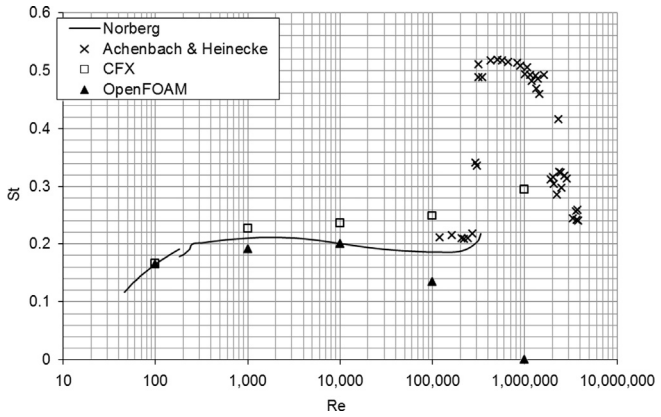

Fig. 8. Graph of Strouhal number with Reynolds number. Experimental data: Norberg (2003); Achenbach and Heinecke (1981).

3.4. Strouhal number

The final part of the analysis considers the Strouhal number of captured vortex shedding. The Strouhal number is an important indicator of the transient accuracy of the simulation. The results in Fig. 8 for CFX and OpenFOAM are compared with an experimental 'best fit' curve from Norberg (2003) and experimental results at high Re from Achenbach and Heinecke (1981). Success in the laminar range continues as the Strouhal number is captured by both codes to an accuracy of ±0.1% compared with experiment. Both codes are within ±9% of findings by Norberg at Re=1000; above this point the CFX simulations begin to shed vortices at steadily increasing rates, failing to predict the drop at intermediate Re values. OpenFOAM provides a matching Strouhal frequency at $Re=10^4$, before a distinct drop at 10^5 and failure to shed at 10^6. With both solvers failing to predict the sharp rise in the super-critical region, it is clear that the SST model is no longer able to produce a realistic flow field. The sharp rise indicates the transition of the boundary layer to a turbulent state; this dramatically reduces the length scale of eddies below the resolution of URANS method. However, although the shedding can no longer be realistically captured, we have previously seen the drag and lift coefficients being predicted with satisfactory accuracy by CFX. One may postulate that the URANS averaging of the more highly turbulent flow is more suited to the CFX model than the structured shedding at lower Re values. Paradoxically OpenFOAM fails to shed, with the previous C_{Lrms} value at 10^6 being accurate by chance rather than realistic flow conditions.

3.5. Pressure coefficient

The variance between the two solvers can be visualised by considering the pressure distribution in the wake. Fig. 9 displays contours of instantaneous pressure coefficient for the CFX and OpenFOAM results at $Re=10^4$. While the general structure of the wake is well matched between plots, the minimum pressure is significantly different. The general range of pressure coefficient is from 1, at regions of stagnation, to 0 at values equal to the free stream pressure, to values <1 for regions of low pressure. With a peak low pressure coefficient of -2.4, CFX predicts pressures 65% lower than OpenFOAM values at vortex centres, as highlighted by arrows in Fig. 9. This difference is inherently connected to the level of vorticity and in turn to shear profile. The pressure variance explains why the lift coefficient is significantly higher for CFX particularly in the sub-critical region. A possible cause of the extreme values is that this region is prone to strongly 3D wakes with distinct laminar shedding modes and transverse flows. This reasoning is supported by Norberg (2003), in which Re is plotted

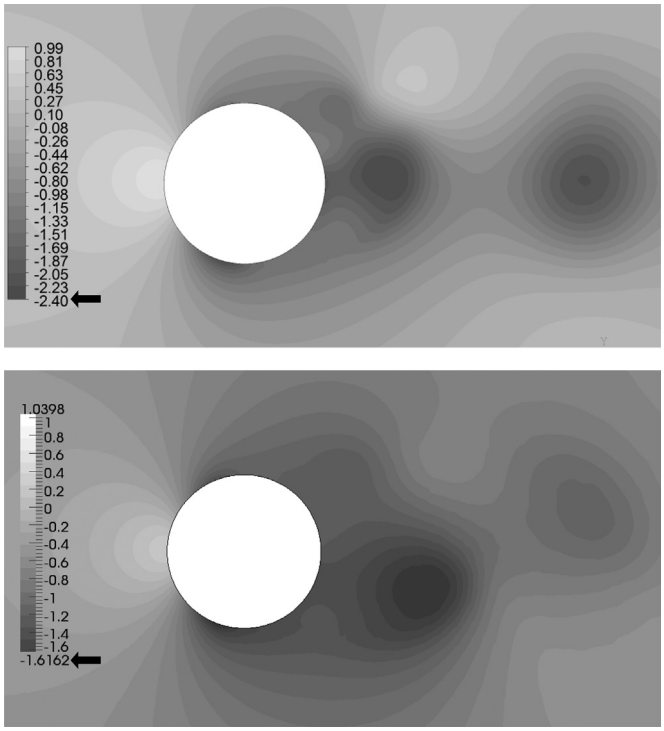

Fig. 9. Contour plots of pressure coefficient for $Re=10^4$; top: CFX and bottom: OpenFOAM.

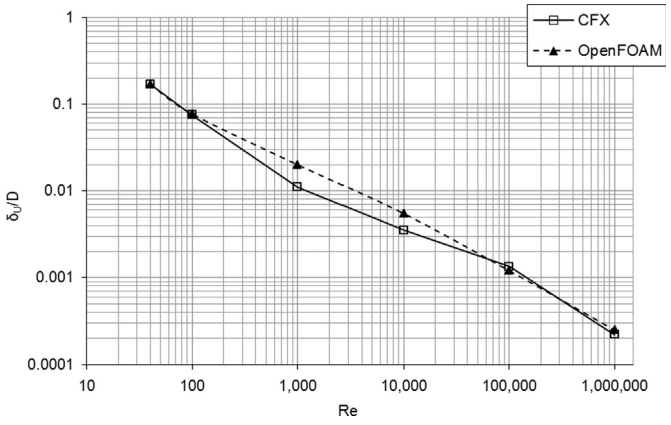

Fig. 10. Graph of non-dimensional minimum boundary layer thickness versus Reynolds number.

against axial correlation length normalised with the diameter (Λ/d). The plot reveals a peak in spanwise flow at $Re\approx 5\times 10^3$, reducing from this point as Re increases. This theory opposes the satisfactory results from OpenFOAM both in terms of forces and shedding frequency. However, a number of reasons may explain this disparity, including, but not limited to, solver specific minimum turbulence levels, density of integration points or variation in the wall handling (see Section 2– Turbulence properties).

3.6. Boundary layer

With boundary layer thickness not known a priori, iterative meshing is required in order to satisfy established values of y^+ and cell count at the non-slip surface. Fig. 10 plots the non-dimensional value of 99% velocity boundary layer thickness (δ_U) divided by cylinder diameter (D), against Reynolds number. While results differ slightly between solvers, the results show a

consistent rate of decay in velocity boundary layer thickness with increasing Re; this relationship was confirmed by solving two other cylinder regimes. Using a trend line approximation a power law can be established to describe the link between Re and δ_U/D, see Eq. (20). The approximation tracks the OpenFOAM result more closely due to the higher solution accuracy produced at sub-critical values, and is proposed as guidance for numerical modelling of smooth circular cylinders.

$$\delta_U/D \cong 1.5Re^{-0.625} \tag{20}$$

4. Conclusions

The aim of the research presented was to perform a robust assessment of the URANS method over a wide range of Reynolds numbers within the limits of a 2D simplification. Success is judged by comparison of forces and transient flow field parameters with experimental values in literature. Two finite volume solvers have been employed and compared; ANSYS® CFX-13.0 and OpenFOAM® 1.7.1. To extract the best possible outcome for the circular cylinder case, a high resolution methodology was established with regard to geometric, numerical and dicrestisation practices which were applied to all cases. Specifically this includes:

- application of URANS calculation using SST turbulence model;
- domain size/cylinder ratio chosen to avoid blockage effects;
- surface meshing to specified y^+ and cell count in boundary layer;
- cell aspect ratio conformity and far field size limitation;
- utilising fully adaptive Courant controlled timestepping;
- maintaining maximum commonality between solvers;

Although previous studies have found successful application of the URANS method for some of the Reynolds numbers considered here, a clear methodology for all flow cases has not previously been proposed and evaluated. For low Reynolds numbers, $Re < 10^3$, the method developed in the present research is highly accurate with both solvers achieving correlation with experiment. At subcritical Reynolds numbers, $Re < 10^5$, the findings are less conclusive. Use of two solvers has exposed fundamental differences despite closely matched definitions for this Re region. While the differences and possible causes have been discussed in the results section of this paper, further work is required to establish exact root causes. However, despite the unavoidable subtle differences between the two setups, OpenFOAM delivers significantly closer values for coefficients of lift, drag and shedding frequency when compared to experiment.

At the onset of drag crisis, considered as the critical region for $10^5 < Re < 10^7$, CFX agrees with findings from published work, such as Ong et al. (2009), achieving high correlation with experimental values for force coefficients, but fails to capture a realistic wake. The pisoFoam solver does not follow this trend, failing to shed at critical Re values. Further work has already included reducing the timestep to a Courant of 0.1 in order to reduce any instability which may result from the absence of under-relaxation. However this provided no change to the result, pointing to a possible issue with the accumulation of numerical truncation errors or the like. The implementation of an Algebraic Multi-Grid (AMG), or solution using pimpleFoam, a solver capable of outer loop time-stepping, may improve high Re convergence in OpenFOAM.

Fundamentally the simplification of the case to 2D and use of a Reynolds-averaged method means that applicability falls predominantly in the subcritical flow region, with OpenFOAM providing values suitable for engineering activities. Above this value LES is advised for fully capturing the forces and wake as demonstrated by alternative publications. Having formed differing conclusions for each solver tested, it is clear that individual benchmarking of software is an essential step for any simulation, a requirement heightened in this case with increasing boundary layer and wake turbulence.

The overall research provides both an insight into the limits of URANS for modelling of circular cylinders and a benchmark for further studies where comparable methods and software are used. As part of this the plot of non-dimensional velocity boundary layer thickness versus Re, and associated relationship given in Eq. (20), is given to assist further numerical studies in RANS and LES where resolution of the boundary layer down to sublayer accuracy is desired.

Acknowledgements

This study is part of a Ph.D. funded by the EPSRC, who are duly thanked for their support.

References

Achenbach, E., 1968. Distribution of local pressure and skin friction around a circular cylinder in cross-flow up to re=5×10^6. J. Fluid Mech. 34 (625-&).
Achenbach, E., Heinecke, E., 1981. On vortex shedding from smooth and rough cylinders in the range of reynolds-numbers 6×10^3 to 5×10^6. J. Fluid Mech. 109, 239–251.
ANSYS®, 2010. Academic Research, Release 13.0, Help system, CFX Reference Guide, 6.3.4.1.5.2: Integration to the wall (low-reynolds number formulaton).
Bardina, J.E., Huang, P.G., Coakley, T.J., 1997. Turbulence Modeling Validation Testing and Development. NASA Technical Memorandum, *110446*.
Benim, A.C., Cagan, M., Nahavandi, A., Pasqualotto, E., 2007. RANS predictions of turbulent flow past a circular cylinder over the critical regime. In: *Proceedings of the 5th Iasme/Wseas International Conference on Fluid Mechanics and Aerodynamics (Fma '07)*, pp. 235–240.
Blazek, J., 2005. Computational Fluid Dynamics: Principles and Applications. Elsevier, Amsterdam; London.
Coutanceau, M., Bouard, R., 1977. Experimental-determination of main features of viscous-flow in wake of a circular-cylinder in uniform translation. 2. Unsteady-flow. J. Fluid Mech. 79, 257.
Dehkordi, B.G., Jafari, H.H., 2009. Numerical simulation of flow through tube bundles in in-line square and general staggered arrangements. Int. J. Num. Methods Heat Fluid Flow 19, 1038–1062.
Dennis, S.C.R., Chang, G.Z., 1970. Numerical solutions for steady flow past a circular cylinder at reynolds numbers up to 100. J. Fluid Mech. 42, 471.
ESDU, 1980. Mean Forces, Pressures and Flow Field Velocities for Circular Cylindrical Structures: Single Cylinder with Two-Dimensional Flow.
Gretton, G.I., 2009. The Hydrodynamic Analysis of a Vertical Axis Tidal Current Turbine (Ph.D. thesis). The University of Edinburgh.
Grove, A.S., Shair, F.H., Petersen, E.E., Acrivos, A., 1964. An experimental investigation of the steady separated flow past a circular cylinder. J. Fluid Mech. 19 (60-&).
Iaccarino, G., Ooi, A., Durbin, P.A., Behnia, M., 2003. Reynolds averaged simulation of unsteady separated flow. Int. J. Heat Fluid Flow 24, 147–156.
Issa, R.I., 1986. Solution of the implicitly discretized fluid-flow equations by operator-splitting. J. Comput. Phys. 62, 40–65.
Jagadeesh, P., Murali, K., 2009. Application of low-Re turbulence models for flow simulations past underwater vehicle hull forms. J. Nav. Archit. Mar. Eng., 2.
Kalitzin, G., Medic, G., Iaccarino, G., Durbin, P., 2005. Near-wall behavior of RANS turbulence models and implications for wall functions. J. Comput. Phys. 204, 265–291.
Lienhard, J.H., 1966. Synopsis of Lift, Drag, and Vortex Frequency Data for Rigid Circular Cylinders. Research Division Bulletin, Washington State University College of Engineering , 32.
Massey, B.S., 1989. Mechanics of Fluids. Van Nostrand Reinhold.
Menter, F.R., 1994. 2-equation eddy-viscosity turbulence models for engineering applications. AIAA J. 32, 1598–1605.
Norberg, C., 2003. Fluctuating lift on a circular cylinder: review and new measurements. J. Fluids Struct. 17, 57–96.
Ong, M.C., Utnes, T., Holmedal, L.E., Myrhaug, D., Pettersen, B., 2009. Numerical simulation of flow around a smooth circular cylinder at very high reynolds numbers. Mar. Struct. 22, 142–153.
Park, J., Kwon, K., Choi, H., 1998. Numerical solutions of flow past a circular cylinder at reynolds numbers up to 160. J. Mech. Sci. Technol. 12, 1200–1205.
Raghavan, K., Bernitsas, M.M., 2011. Experimental investigation of reynolds number effect on vortex induced vibration of rigid circular cylinder on elastic supports. Ocean Eng. 38, 719–731.
Rahman, M.M., Karim, M.M., Alim, M.A., 2008. Numerical investigation of unsteady flow past a circular cylinder using 2-d finite volume method. J. Nav. Archit. Mar. Eng., 4.

Roshko, A., 1955. On the wake and drag of bluff bodies. J. Aeronaut. Sci. 22, 124–132.
Shih, W.C.L., Wang, C., Coles, D., Roshko, A., 1993. Experiments on flow past rough circular-cylinders at large reynolds-numbers. J. Wind Eng. Ind. Aerodyn. 49, 351–368.
Spalding, D.B., 1961. A single formula for the law of the wall. Trans ASME Series A: J. Appl. Mech. 28, 444–458.
Taneda, S., 1956. Experimental investigation of the wakes behind cylinders and plates at low reynolds numbers. J. Phys. Soc. Jpn. 11, 302–307.
Tritton, D.J., 1959. Experiments on the flow past a circular cylinder at low reynolds numbers. J. Fluid Mech. 6, 547.
Tutar, M., Holdo, A.E., 2001. Computational modelling of flow around a circular cylinder in sub-critical flow regime with various turbulence models. Int. J. Num. Methods Fluids 35, 763–784.
Wieselsberger, C., 1923. Ergebnisse der aerodynamischen versuchsanstalt zu gottingen, unter mitwirkung von… C. Wieselsberger und… A. Betz herausgegeben von… L. Prandtl,… I.[-ii.] lieferung.
Wilcox, D.C., 1993. A two-equation turbulence model for wall-bounded and free-shear flows. In: Proceedings of the AIAA 24th Fluid Dynamics Conference, AIAA, Orlando, FL.
Williamson, C.H.K., 1996. Vortex dynamics in the cylinder wake. Annu. Rev. Fluid Mech. 28, 477–539.
Xia, J.Q., Falconer, R.A., Lin, B.L., 2010. Impact of different operating modes for a severn barrage on the tidal power and flood inundation in the severn estuary, UK. Appl. Energy 87, 2374–2391.
Zdravkovich, M.M., 1990. Conceptual overview of laminar and turbulent flows past smooth and rough circular-cylinders. J. Wind Eng. Ind. Aerodyn. 33, 53–62.